magnetochemistry

MDPI

Article

Series of Chloranilate-Bridged Dinuclear Lanthanide Complexes: Kramers Systems Showing Field-Induced Slow Magnetic Relaxation †

Ryuta Ishikawa [1,*], Shoichi Michiwaki [1], Takeshi Noda [1], Keiichi Katoh [2], Masahiro Yamashita [2,3,4] and Satoshi Kawata [1]

1 Department of Chemistry, Faculty of Science, Fukuoka University, 8-19-1 Nanakuma, Jonan-ku, Fukuoka 814-0180, Japan; sd142022@cis.fukuoka-u.ac.jp (S.M.); sd172011@cis.fukuoka-u.ac.jp (T.N.); kawata@fukuoka-u.ac.jp (S.K.)
2 Department of Chemistry, Graduate School of Science, Tohoku University, 6-3 Aza-Aoba, Aramaki, Aoba-ku, Sendai, Miyagi 980-8578, Japan; kkatoh@m.tohoku.ac.jp (K.K.); yamasita@agnus.chem.tohoku.ac.jp (M.Y.)
3 Advanced Institute for Materials Research (AIMR), Tohoku University, 2-1-1 Katahira, Aoba-ku, Sendai, Miyagi 980-8577, Japan
4 School of Materials Science and Engineering, Nankai University, Tianjin 300350, China
* Correspondence: ryutaishikawa@fukuoka-u.ac.jp; Tel.: +81-92-871-6631
† This manuscript is dedicated to Professor Masahiro Yamashita on the occasion of his 65th birthday for his contributions to the multifunctional nanosciences of advanced coordination compounds.

Received: 26 March 2019; Accepted: 18 April 2019; Published: 2 May 2019

Abstract: A series of chloralilate-bridged dinuclear lanthanide complexes of formula $[\{Ln^{III}(Tp)_2\}_2(\mu\text{-}Cl_2An)]\cdot 2CH_2Cl_2$, where Cl_2An^{2-} and Tp^- represent the chloranilate and hydrotris (pyrazolyl)borate ligands, respectively, and Ln = Gd (**1**), Tb (**2**), Ho (**3**), Er (**4**), and Yb (**5**) was synthesized. All five complexes were characterized by an elemental analysis, infrared spectroscopy, single crystal X-ray diffraction, and SQUID measurements. The complexes **1**–**5** in the series were all isostructural. A comparison of the temperature dependence of the dc magnetic susceptibility data of these complexes revealed clear differences depending on the lanthanide center. Ac magnetic susceptibility measurements revealed that none of the five complexes exhibited a slow magnetic relaxation under a zero applied dc field. On the other hand, the Kramers systems (complexes **4** and **5**) clearly displayed a slow magnetic relaxation under applied dc fields, suggesting field-induced single-molecule magnets that occur through Orbach and Raman relaxation processes.

Keywords: lanthanide ions; slow magnetic relaxation; single-molecule magnets

1. Introduction

Single-molecule magnets (SMMs) and single-ion magnets (SIMs), comprising molecules with a one spin center, have attracted significant attention as potential candidates for molecule-based electronic applications such as high-density information storage [1], quantum computing [2–5], and spintronic devices [6–9]. For the realization of such applications, a very large barrier height and a high blocking temperature for the reorientation of the magnetic moment must be achieved. The barrier height and blocking temperature in SMMs and SIMs depend on two key factors, namely, a significant magnetic anisotropy and large number of spins. Thus, the high magnetic anisotropy and large number of spins per ion make lanthanide(III) ions (Ln^{III}) highly suitable for application in SMMs and SIMs. In fact, the development of SMMs and SIMs based on Ln complexes is on the rise [10–18]. These Ln^{III}-based SMMs and SIMs generally display very high barrier heights and blocking temperatures over those

of the representative cluster-type SMM $[Mn^{III}_8Mn^{IV}_4O_{12}(CH_3COO)_{16}(H_2O)_{24}]\cdot 2CH_3COOH\cdot 4H_2O$, which is based on first-row transition metal ions [19,20].

Recently, chloralilate (Cl_2An^{2-}) bridged dinuclear Ln^{III} complexes of the formula $[\{Ln^{III}(Tp)_2\}_2(\mu\text{-}Cl_2An)]\cdot 2CH_2Cl_2$ (Tp^- = hydrotris(pyrazolyl)borate) have been reported in the literature [21–24]. In these complexes, the Dy^{III} analogue displays a slow magnetic relaxation under small applied dc magnetic fields, thus behaving as a field-induced SMM [22–24]. This paper reports the syntheses, structures, and magnetic properties of a series of Cl_2An^{2-} bridged dinuclear Ln complexes of the formula $[\{Ln(Tp)_2\}_2(\mu\text{-}Cl_2An)]\cdot 2CH_2Cl_2$ [Ln = Gd (**1**), Tb (**2**), Ho (**3**), Er (**4**), and Yb (**5**)] to systematically investigate the magnetic properties in other Ln^{III} analogues of $[\{Ln^{III}(Tp)_2\}_2(\mu\text{-}Cl_2An)]\cdot 2CH_2Cl_2$.

2. Results and Discussions

2.1. Structural Descriptions

The series of Cl_2An^{2-} bridged neutral dinuclear Ln^{III} complexes **1**–**5** were prepared by a slight modification of the original method reported by Kaizaki et al. [21]; some of these complexes have been previously reported [22–24]. All the complexes were isolated as X-ray quality single crystals through several recrystallizations from a concentrated dichloromethane solution layered with hexane. The purity of these freshly prepared single crystals was confirmed by an elemental analysis.

A single-crystal X-ray diffraction (SCXRD) analysis showed **1**–**5** crystallizing as an isostructural series in the monoclinic space group $P2_1/n$ (No.14), with an asymmetric unit containing half of the dinuclear complexes and one CH_2Cl_2 molecule as the lattice solvent (Figure 1 and Table S1). Consequently, the unit cell comprises two complete dinuclear complexes and two lattice CH_2Cl_2 solvents. An inversion center is located at the midpoint of the central bis-bidentate Cl_2An^{2-} bridging ligand, rendering the two Ln^{III} centers equivalent by symmetry. In all five complexes, the coordination environments around the Ln^{III} centers are eight-coordinated with six N atoms from the two Tp^- capping ligands and two O atoms from the bridging Cl_2An^{2-} ligand. The average Ln–O and Ln–N distances of complexes **1**–**5** are in the ranges of 2.330(2) to 2.398(3) Å and 2.446(2) to 2.514(3) Å, respectively (Table 1), and are in agreement with previously reported values for other Ln-based complexes [10–18]. For all five complexes, the Ln–O distances are ≤0.12 Å shorter than the Ln-N distances, since the O atoms in the bridging Cl_2An^{2-} ligand exhibit a larger negative partial charge than the N atoms in the Tp^- ligand. A comparison of the bond distances in **1**–**5** reveals a slight decrease in the average Ln–O and Ln–N distances, from left to right across the isostructural series, as expected from the change in the ionic radii. This systematic decrease is evidence of the lanthanide contraction phenomenon [25–28].

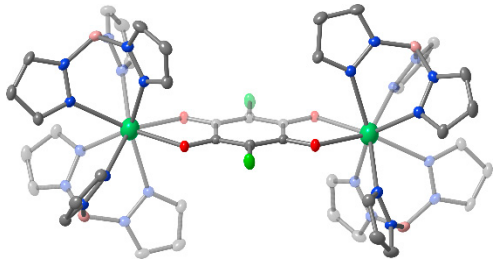

Figure 1. Solid state molecular structure of $[\{Ln(Tp)_2\}_2(\mu\text{-}Cl_2An)]\cdot 2CH_2Cl_2$ with thermal ellipsoids drawn at a 50% probability level with the exception of lanthanide atoms shown at a 99% probability level. The spring green, blue, red, sundown, vivid lime green, and gray ellipsoids represent Ln, N, O, B, Cl, and C atoms, respectively. Hydrogen atoms and lattice solvent molecules are omitted for clarity.

Table 1. Selected bond distances [1] (Å) for **1**–**5**.

	Ln–O [2]	Ln–N [2]	Intramolecular Ln···Ln [3]	Intermolecular Ln···Ln [4]
1	2.398(3)	2.514(3)	8.7042(5)	8.7420(5)
2	2.375(3)	2.492(3)	8.661(2)	8.703(2)
3	2.363(2)	2.482(2)	8.6424(5)	8.7308(4)
4	2.348(2)	2.465(2)	8.6084(9)	8.699(1)
5	2.330(2)	2.446(2)	8.5599(9)	8.671(1)

[1] Note that the single crystal X-ray diffraction data for **1**–**5** were collected at different temperatures. [2] Averages of crystallographically independent Ln–O and six Ln–N values. [3] Symmetry code: $-x + 1, -y + 1, -z + 2$. [4] Closest separation.

The coordination geometry and environment around the Ln^{III} centers have a significant influence on the electronic structure and magnetic anisotropy. To determine the coordination geometries of the Ln^{III} centers for **1**–**5**, continuous shape measurements (CShM) were determined using the SHAPE Version 2.1 software [29,30], where two Ln^{III} centers are related by inversion symmetry and therefore possess the same coordination geometry (vide supra). Based on the resultant SHAPE indices (0.722–0.831 for **1**–**5**; Table 2), the eight-coordinate Ln^{III} centers of **1**–**5** are best described as having slightly distorted triangular dodecahedral geometries.

Table 2. Summary of SHAPE parameters [1] for lanthanide centers in the series of the dinuclear complexes **1**–**5**.

	SAPR [2]	TDD [3]	BTBR [4]
1	2.320	0.831	1.788
2	2.291	0.809	1.774
3	2.199	0.764	1.728
4	2.215	0.749	1.732
5	2.189	0.722	1.707

[1] A shape index equal to zero represents an ideal geometry. [2–4] SAPR, TDD, and BTBR are square antiprismatic, triangular dodecahedral, and bi-augmented trigonal prismatic geometries, respectively.

The bond distances within the quinoidal rings (e.g., Cl_2An^{2-} ligand) bound to the Ln^{III} centers provide strong information on the electronic structures of the ligands. The average C–O and C–C distances, with the delocalized bonding in the Cl_2An^{2-} rings of **1**–**5**, are in the range 1.252(4)–1.260(5) Å and 1.390(5)–1.394(4) Å, respectively, while the C–C distances with single bonding are in the range of 1.532(4)–1.542(4) (Table 3). The bond distances within the quinoidal rings of the bridging Cl_2An^{2-} ligands fall within the same error over **1**–**5**, which all adopt bi-separated delocalized forms [23]. These results are strongly supported by the infrared (IR) spectral data (Scheme 1).

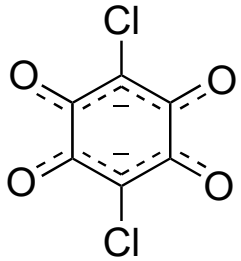

Scheme 1. Bi-separated delocalized structure of Cl_2An^{2-} in **1**–**5**.

Table 3. Selected bond distances [1] (Å) for the Cl_2An^{2-} moiety in **1**–**5**.

	C–O [2]	C–C [2]	C–C [3]
1	1.259(4)	1.391(5)	1.537(4)
2	1.252(4)	1.390(5)	1.542(4)
3	1.258(3)	1.394(3)	1.537(3)
4	1.256(3)	1.392(4)	1.534(4)
5	1.253(3)	1.393(4)	1.532(4)

[1] Bonds are shown in detail in Scheme 1. [2] Averages of two crystallographically independent delocalized C–O and C–C values. [3] Values of the C–C single bond moiety.

For complexes **1**–**5**, the respective intramolecular $Ln^{III}\cdots Ln^{III}$ separations through the Cl_2An^{2-} bridges are in the range of 8.5599(9)–8.7042(5) Å, whereas the closest intermolecular $Ln^{III}\cdots Ln^{III}$ separations, which are in the range of 8.671(1)–8.7420(5) Å, are comparable with the intramolecular distances (Table 1). These close intra- and intermolecular $Ln^{III}\cdots Ln^{III}$ distances may lead to magnetically dipolar interactions, which could create a small bias that allows for the quantum tunneling of the magnetization at the zero field (vide infra).

2.2. Infrared Spectroscopy

The IR spectra of **1**–**5** provide complementary structural feature information to that obtained by SCXRD analysis (Figure S1). The IR vibrations associated with the bridging Cl_2An^{2-} ligand in the five complexes are typified by predominant C–Cl and C–O vibrations at ~850 and 1530 cm^{-1}, respectively [22–24]. These results are a promising indication that the Cl_2An^{2-} ligand in complexes **1**–**5** is in a bi-separated delocalized form [22–24,31]. Furthermore, the presence of the ancillary Tp^- ligands in complexes **1**–**5** is confirmed by characteristic vibrations at ~2470 cm^{-1} (c.f., Tp^-, ν_{BH} = ~2440 cm^{-1}) [22–24,32]. The predominant contributions to the vibrational modes are from the skeleton of the ligand and, thus, there are no significant differences in the IR spectra. The changes in the atomic weight of the Ln^{III} centers are reflected in the specific peak shifts of the IR spectra. For the five complexes, the most notable change is observed in the Ln–O vibrations at ~460 cm^{-1}, where the Ln–O vibrational peak shifts to a higher energy (453–466 cm^{-1}) with an increasing atomic number. This increase can be explained by the lanthanide contraction effect.

2.3. Magnetic Properties

2.3.1. Static Magnetic Properties

For all of the dinuclear complex series (**1**–**5**), the temperature (T) dependence of the dc magnetic susceptibility (χ_M) data was collected under an applied dc field of 0.1 T in the temperature range of 1.8–300 K. A comparison of the resulting $\chi_M T$ versus T data reveals marked differences between the dc magnetism of complexes **1**–**5**. The $\chi_M T$ values at 300 K for **1**–**5** (15.73, 22.80, 27.97, 22.44, and 5.12 cm^3 K mol^{-1}, respectively) are in good agreement with the expected values (15.75, 23.63, 28.13, 22.95, and 5.14 cm^3 K mol^{-1}, respectively) for two non-interacting Ln^{III} centers. The $\chi_M T$ products for complexes **2**–**5** gradually decreased over the temperature range of 300–50 K. Subsequently, they rapidly decreased below 50 K and finally reached values of 15.02, 8.91, 4.47, 13.32, and 2.50 cm^3 K mol^{-1}, respectively, at 1.8 K, due to the depopulation of the excited crystal field state. For complexes **2**–**5,** the isothermal dc magnetization at 1.8 K increased steeply with an increasing magnetic field at low magnetic field regions before increasing linearly in high magnetic field regions, finally reaching respective values of 9.63, 11.51, 9.32, and 3.85 μ_B at 7 T without saturation, indicating very strong magnetic anisotropy (Figure 2b). Moreover, no hysteresis was observed for **2**–**5**, even at 1.8 K using a conventional superconducting quantum interference device (SQUID). This suggests that the static magnetic behavior observed for **2**–**5** arose from significant spin-orbit coupling interactions and a strong unquenched orbital angular momentum. On the other hand, **1** comprises a half-filled 4f shell. Thus, its ground state has no orbital angular momentum and can be considered a spin-only system. In this case, the first-order effect of the

spin-orbit coupling disappears for the ground electronic term $^8S_{7/2}$, and magnetic anisotropy is caused by the second-order effect of the spin-orbit coupling; this is known as zero-field splitting. The $\chi_M T$ value of 15.73 cm^3 K mol^{-1} at 300 K observed for **1** is in good agreement with the expected values (15.75 cm^3 K mol^{-1}) for two non-interacting Gd^{III} centers. The $\chi_M T$ product for **1** remains essentially constant down to 10 K and then gradually decreases to 15.02 cm^3 K mol^{-1} at 1.8 K. The magnetization curve of **1** at 1.8 K was saturated at 14 μ_B at 7 T, confirming that **1** is in the ground state of $^8S_{7/2}$.

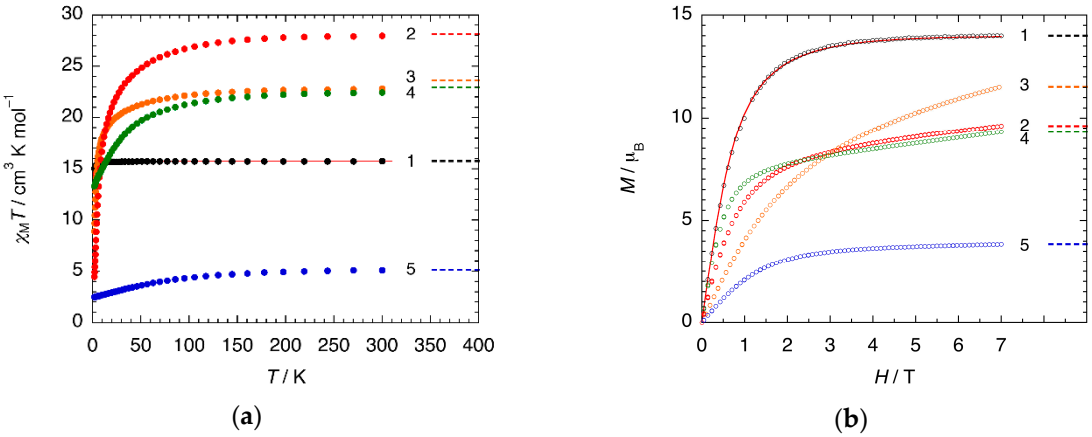

Figure 2. (**a**) Temperature dependence of the molar magnetic susceptibility times the temperature for **1**–**5** over the temperature range between 1.8 and 300 K under an applied dc field of 0.1 T; (**b**) Field dependence of molar magnetization for **1**–**5** over the dc field range between 0 and 7 T at 1.8 K. The broken lines correspond to ideal free-ion values. The solid red lines represent fits to the experimental data using the spin Hamiltonian based on the zero-field splitting, which has been previously described in detail [23].

2.3.2. Dynamic Magnetic Properties

To study the possibility of a slow magnetic relaxation, the ac susceptibility measurements for **1**–**5** were performed at 1.8 K with a dc magnetic field in the range of 0–0.3 T. The out-of-phase ac susceptibility (χ_M'') signals for all five complexes in the absence of an applied field did not present any apparent peaks in the available frequency (ν) range. As expected for the eight-coordinated triangular dodecahedral geometry of the two Ln^{III} centers, an approximate D_{2d} symmetry was observed. This led to the crystal field parameters $B^0{}_2$, $B^0{}_4$, $B^4{}_4$, $B^0{}_6$, and $B^4{}_6$, wherein $B^4{}_4$ and $B^4{}_6$ are the off-diagonal components. The existence of these off-diagonal crystal field parameters strongly suggests the mixing of the ground M_J states. Furthermore, the Ln^{III} centers in **1**–**5** comprise isotopes that display a nuclear spin, resulting in the nuclear hyperfine interaction effect [33–37]. Additionally, the intra- and/or intermolecular separations between the Ln^{III} centers suggests the presence of dipolar interactions [10–18]. These contributions lead to the absence of a slow magnetic relaxation under a zero applied dc field, thereby allowing the quantum tunneling of the magnetization. In such cases, the application of a dc field can suppress and break up the quantum tunneling, caused by nuclear hyperfine couplings, dipolar interactions, and transverse fields from the off-diagonal crystal field splittings, and reveal the slow relaxation of the magnetization. However, under small static dc magnetic fields, frequency-dependent non-zero χ_M'' signals were only clearly observed for the Kramers ions in complexes **4** and **5** (Figure 3, Figures S2 and S3). For these two complexes, each χ_M'' peak maximum shifted to a lower frequency with an increasing applied dc field ≤0.1 T. A further increase in the applied dc field resulted in the maximum χ_M'' shifting to a higher frequency. Notably, **4** and **5** also presents another minor magnetic relaxation process at higher dc fields (Figure 3), which may arise from thermally assisted quantum tunneling [10–18]. The dc field dependence of the low temperature relaxation times ($\tau = 1/2\pi\nu$) for **4** and **5** was extracted at each of these fields by fitting ν versus χ_M' and χ_M'' and the Argand plots [38,39] (χ_M' versus χ_M'') using a generalized Debye model [40]. The values

determined for **4** and **5** are listed in Tables S2 and S3 and plotted in Figure S3. The two magnetic relaxation processes of the direct and quantum relaxation pathways were elucidated by fitting the variable-field magnetic relaxation data of **4** and **5** using Equation (1) [10–18]:

$$\tau^{-1} = AH^nT + \frac{B_1}{1 + B_2H^2} \quad (1)$$

where the first and second terms represent the respective direct and quantum tunneling pathways. Moreover, because of the presence of Kramers ions, the power index $m = 4$ was used for the direct process. The best fits, based on Equation (1), are presented as solid black lines in Figure 3 and are summarized in Table 4. These results imply that the dipolar interactions and/or off-diagonal crystal fields support quantum tunneling at low magnetic dc fields. On the other hand, due to the presence of spin-active nuclei, single-phonon direct relaxation dominates at high dc fields. In addition, the optimum dc field for **4** and **5** was determined as ~0.1 T.

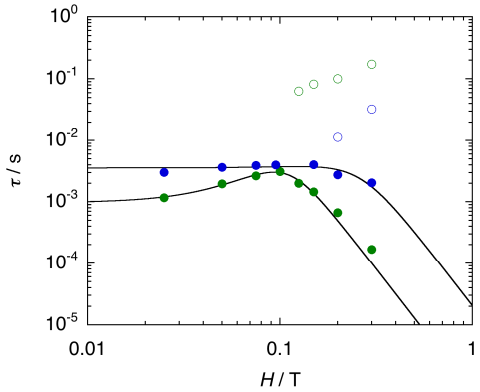

Figure 3. Comparison of the field-dependent relaxation time (τ) at 1.8 K for two distinct major (filled circles) and minor (open circles) relaxations observed for **4** (green), and **5** (blue). The solid black lines represent fits to the experimental data using the appropriate magnetic relaxation pathways considering both the quantum tunneling and direct processes (Equation (1)).

Table 4. Summary of field-dependent ac magnetic data [1] for 4 and 5.

	A (s^{-1} K^{-1} T^{-4})	B_1 (s^{-1})	B_2 (T^{-2})
4	6.80×10^5	1.03×10^3	3.85×10^2
5	2.70×10^4	2.82×10^2	6.42

[1] Data measured at 1.8 K.

Subsequently, ac susceptibility measurements were performed under an applied dc field of 0.1 T in the temperature range of 1.8–10 K (Figure 4), where the optimum dc magnetic field for **4** and **5** was determined as 0.1 T (variable-field magnetic relaxation data; vide supra, Figure 3). The temperature dependences of the magnetic relaxation times for **4** and **5** were extracted in the temperature range of 1.8–5.0 K by fitting ν versus χ_M' and χ_M'' and the Argand plots using a generalized Debye model (Figures 4 and 5, and Tables S4 and S5, respectively). The Argand plots for **4** and **5** comprised one semicircle with small α parameters in the ranges of 0.08–0.42 (4) and of 0.02–0.18 (5).

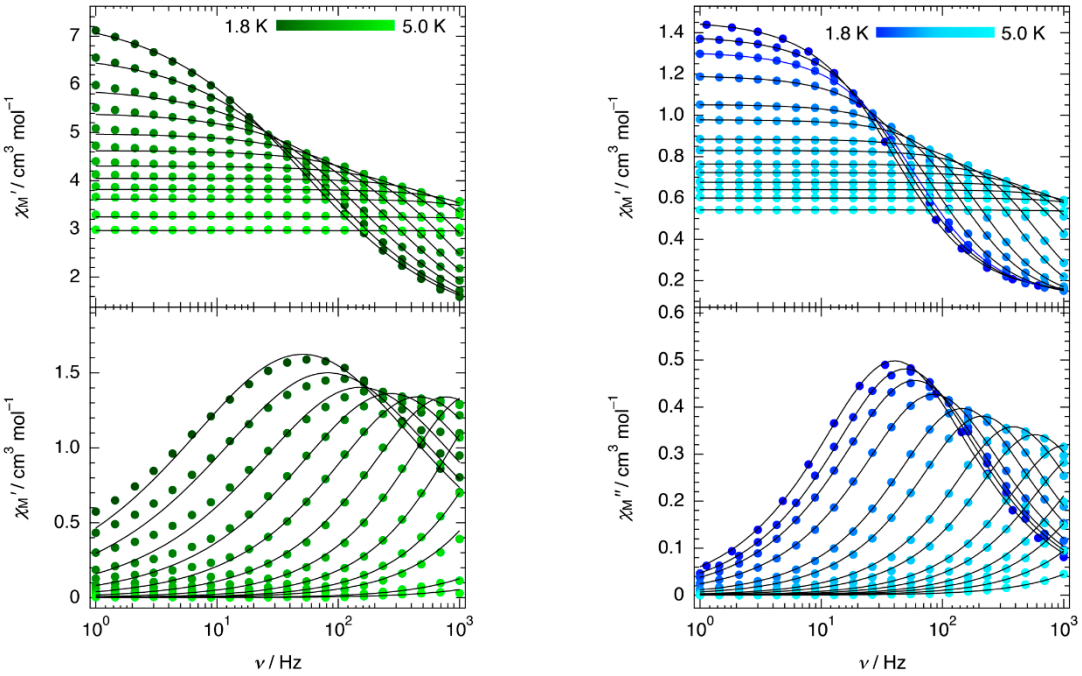

Figure 4. Frequency dependence of the molar in-phase (top) and out-of-phase (bottom) susceptibility for (**a**) **4** and (**b**) **5** over the frequency 1–1000 Hz and the temperature range 1.8–5.0 K in a 2.5 Oe ac field under an applied dc field of 0.1 T. The solid black lines represent fits to the experimental data using the generalized Debye model with the α parameter in the ranges of 0.08–0.42 for **4** and of 0.02–0.18 for **5**.

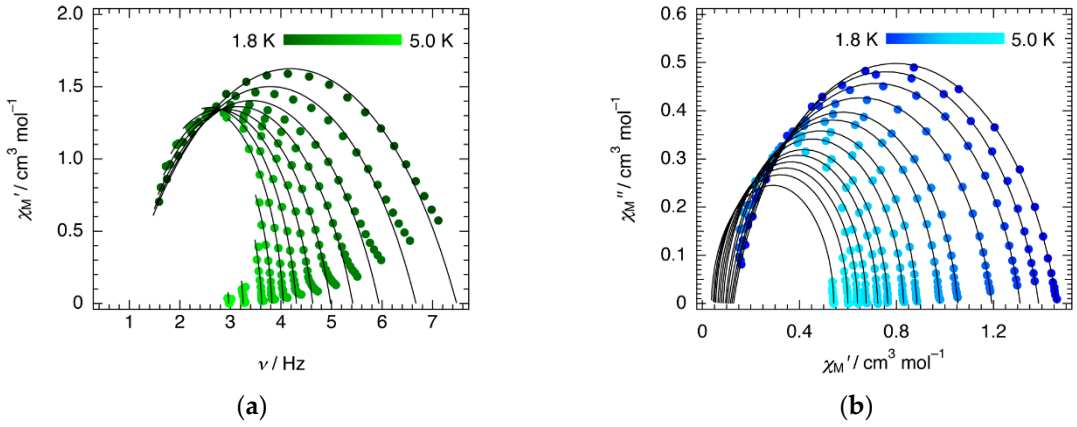

Figure 5. Argand plots for the molar ac susceptibility data of (**a**) **4** and (**b**) **5** in the temperature range 1.8–5.0 K under an applied dc field of 0.1 T. The solid black lines correspond to fits to the experimental data using the generalized Debye model with the α parameter in the ranges of 0.08–0.42 for 4 and of 0.02–0.18 for **5**.

The linear regions at a high temperature in the plots of τ versus $1/T$ (Figure S4) were fitted, assuming an Orbach relaxation (ideal thermal excitation over the energy barrier for the molecule [10–18,40]), as described by Equation (2):

$$\tau^{-1} = \tau_0^{-1} \exp\left(-\frac{\Delta_{\text{eff}}}{k_B T}\right) \quad (2)$$

Arrhenius fits of the temperature-dependent relaxation time afford the thermally activated barriers $\Delta_{\text{eff}} = 26.0\ \text{cm}^{-1}$ ($\tau_0 = 1.79 \times 10^{-9}$ s) for **4** and 21.5 cm^{-1} for **5** ($\tau_0 = 2.81 \times 10^{-8}$ s). The extracted τ_0 values

fall within the typical range of Ln^{III}-based single-molecule and single-ion magnets [10–18]. As the temperature decreases, the plots of τ versus $1/T$ for **4** and **5** become gradually nonlinear (Figure 6). Such behavior suggests the coexistence of multiple magnetic relaxation pathways, which is caused by energy transfer from the spin to the lattice; this is known as the spin-lattice relaxation [10–18]. Hence, the variable temperature relaxation times for **4** and **5** were analyzed in terms of their spin-lattice relaxation (Equation (3)):

$$\tau^{-1} = AH^nT + \frac{B_1}{1 + B_2H^2} + \tau_0^{-1}\exp\left(-\frac{\Delta_{eff}}{k_BT}\right) + CT^m \quad (3)$$

where the first, second, third, and fourth terms represent the direct, quantum tunneling, Orbach, and Raman relaxation processes, respectively [10–18]. Since the temperature dependence of the τ data was collected at the optimum dc field of 0.1 T, the direct and quantum tunneling contributions should be excluded. Therefore, the overall τ versus $1/T$ data for **4** and **5** can only be fit with the Orbach and Raman contributions. The best fits, presented as solid black lines, are illustrated in Figure 6 and Figure S5, while their best-fit parameters are listed in Table 5. The calculated m values are smaller than the ideal value of $m = 9$ for the Kramers ions, suggesting that these Raman-like relaxations are attributed to acoustic and optical vibrations [10–18].

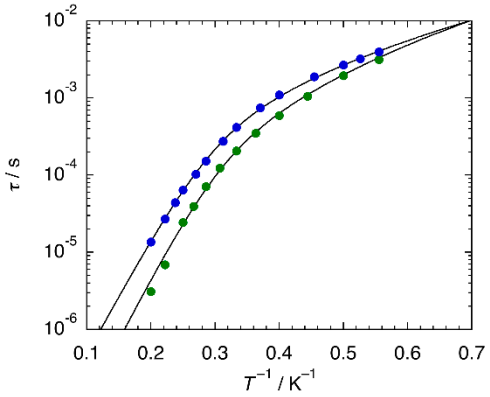

Figure 6. Comparison of the temperature-dependent relaxation under an applied dc field of 0.1 T for **4** (green) and **5** (blue). The solid black lines represent fits to the experimental data using the appropriate magnetic relaxation pathways (Equation (3)).

Table 5. Summary of temperature-dependent ac magnetic data for **4** and **5**.

	τ_0 (s)	Δ_{eff} (cm^{-1})	C (s^{-1} K^{-n})	m
4	3.04×10^{-9}	25.9	17.50	4.84
5	2.68×10^{-8}	22.3	31.39	3.55

2.4. Electrochemistry

The Cl_2An^{2-} ligand could be utilized not only as a bridging unit for designing novel multinuclear coordination assemblies, but also as a non-innocent ligand, namely a reversible redox active ligand. Therefore, utilizing the non-innocent Cl_2An^{2-} as the bridging ligand in SMMs offers the enticing possibility for redox controllable magnetic behavior via an electrical signal. To probe the redox behavior of the field-induced SMMs **4** and **5**, electrochemical measurements were carried out in degassed CH_2Cl_2 with n-Bu_4NPF_6 as the supporting electrolytes. The cyclic voltammogram shows the single quasi-reversible one-electron reduction at $E_{1/2}$ = 1.05 V for **4** and 1.07 V for **5** versus the ferrocene/ferrocenium couple (vs. $Fe(Cp)_2^{0/1+}$), which was assigned as the ligand-based process (Figure S6). The $E_{1/2}$ values of **4** and **5** are similar to those reported for related compounds [22–24]. Attempts and efforts to isolate the one-electron reduced products can be found elsewhere [22–24].

3. Experimental Section

3.1. Materials and Methods

The lanthanide chlorides and solvents were purchased from Wako Pure Chemical Industries, Ltd. (Osaka, Japan). $Na_2Cl_2An{\cdot}3H_2O$ and KTp were purchased from Tokyo Chemical Industry (TCI) Co., Ltd. (Tokyo, Japan). All chemicals were of reagent grade and were used as received. Both CH_2Cl_2 and hexane were of super dehydrated grade. All of the reactions and manipulations were performed under aerobic conditions at an ambient temperature.

3.2. Synthesis of [{Ln(Tp)$_2$}$_2$(μ-Cl$_2$An)]·2CH$_2$Cl$_2$ (Ln = Gd (1), Tb (2), Ho (3), Er (4) and Yb (5))

All the complexes were synthesized according to a previously reported method [21], with modifications. Single crystals suitable for single-crystal X-ray measurements were obtained by recrystallization from CH_2Cl_2/hexane. Notably, several recrystallizations were necessary to obtain samples of sufficient purity. Crystalline yields for each complex were in the range of 38–51%. Anal. Calcd. for $C_{44}H_{44}B_4Cl_6Gd_2N_{24}O_4$: C, 34.24; H, 2.87; N, 21.78%. Found: C, 34.56; H, 2.91, N, 21.94%. Anal. Calcd. for $C_{44}H_{44}B_4Cl_6Tb_2N_{24}O_4$: C, 34.17; H, 2.87; N, 21.73%. Found: C, 34.29; H, 2.88, N, 21.63%. Anal. Calcd. for $C_{44}H_{44}B_4Cl_6Ho_2N_{24}O_4$: C, 33.90; H, 2.85; N, 21.57%. Found: C, 34.12; H, 2.71, N, 21.66%. Anal. Calcd. for $C_{44}H_{44}B_4Cl_6Er_2N_{24}O_4$: C, 33.80; H, 2.84; N, 21.50%. Found: C, 33.81; H, 2.98, N, 21.24%. Anal. Calcd. for $C_{44}H_{44}B_4Cl_6Yb_2N_{24}O_4$: C, 33.55; H, 2.82; N, 21.34%. Found: C, 33.42; H, 2.91, N, 21.55%.

3.3. Single Crystal X-ray Crystallography

The single crystals of **2**–**5** were coated with Nujol, quickly mounted on MicroLoops (MiTeGen LLC., Ithaca, NY, USA), and immediately cooled in a cold N_2 stream to prevent any lattice solvent loss. The data collections were performed on a Rigaku Saturn 724 or R-AXIS RAPID II IP diffractometer (Rigaku Corporation, Tokyo Japan) with graphite-monochromated Mo-*Kα* radiation (λ = 0.71075 Å) and a low-temperature device. The data integration, preliminary data analysis, and absorption collections were performed on a Rigaku CrystalClear-SM 1.4.0 SP1 [41], using the CrystalStructure 4.2.2 [42] crystallographic software packages. The molecular structures were solved by the direct methods included in SIR2011 [43] and refined with the SHELXL [44] program. All non-hydrogen atoms were refined anisotropically. CCDC-1905608–1905611 for **2**–**5** contain the supplementary crystallographic data for this paper and can be obtained free of charge from The Cambridge Crystallographic Data Centre via www.ccdc.cam.ac.uk/data_request/cif. All the hydrogen atoms were included in the calculated positions. Table S1 summarizes the lattice constants and structure refinement parameters for complexes **2**–**5**.

3.4. Physical Measurements

The elemental analysis was performed on a J-Science Lab Micro Corder JM10 (J-Science Lab Co., Ltd., Kyoto, Japan). The Fourier transform infrared spectra were collected using KBr disks, on a JASCO FT/IR-410 spectrometer (JASCO Corporation, Tokyo, Japan) in the range of 400–4000 cm^{-1} at a resolution of 4 cm^{-1} at an ambient temperature. The magnetic data were collected using a Quantum Design MPMS3 SQUID magnetometer (Quantum Design Japan, Inc., Tokyo Japan). The measurements were performed with crushed crystalline samples in a calibrated gelatin capsule. The dc magnetic susceptibility measurements were performed in the temperature range of 1.8–300 K in a dc field of 0.1 T. The field-dependent dc magnetization measurements were performed from −7 to +7 T at 1.8 K. The ac susceptibility measurements were performed in the temperature range of 1.8–15 K in a 2.5 Oe ac field, oscillating at a frequency range of 1–997 Hz in different applied dc fields. The obtained magnetic susceptibility data were corrected for diamagnetic contributions from the sample holder as well as for the core diamagnetism of each sample, estimated from Pascal's constants [45]. The cyclic voltammetric measurements were performed in a 0.1 M CH_2Cl_2 solution of *n*-Bu_4NPF_6 using an

ALS/chi Electrochemical Analyzer Model 610A with a computer-controlled workstation (ALS Co., Ltd, Tokyo, Japan). The solutions contained approximately 1 mM in compounds. The experiments were performed under a continuous flow of N_2 gas using a standard three-electrode cell (platinum working and counter electrodes with an Ag/Ag^+ reference electrode, respectively). The reported potentials are all referenced to the $Fe(Cp)_2^{0/1+}$ couple, which was determined using Fe(Cp) as an internal standard at 0 V.

4. Conclusions and Outlook

The series of Cl_2An^{2-} bridged dinuclear Ln complexes with the formula $[\{Ln(Tp)_2\}_2(\mu\text{-}Cl_2An)]\cdot 2CH_2Cl_2$ (Ln = Gd (1), Tb (2), Ho (3), Er (4), and Yb (5)) were successfully synthesized and systematically characterized by a single X-ray diffraction and by SQUID measurements. All five dinuclear Ln complexes were isostructural and clearly displayed the structural change attributed to the lanthanide contraction effect. A comparison of the dc magnetic data for **1**–**5** revealed clear differences depending on the Ln^{III} centers. None of the five complexes displayed any slow relaxation of the magnetization under a zero applied dc field, while only two complexes (**4** and **5**) presented a slow relaxation of the magnetization in the presence of small dc fields. These two complexes correspond to Kramers ions. The dynamic magnetic properties of **4** and **5** were interpreted by using multiple relaxation pathways, whereby both Orbach and Raman relaxation processes were considered.

The proposed series comprises dinuclear Ln complexes with an electroactive Cl_2An^{2-} bridging ligand. For more potential applications, an important challenge is to switch the slow magnetization phenomena with chemical and physical external fields. These electrochemical molecular switches must be from particularly attractive molecule-based devices, in which the electroactive molecules are reversibly converted between different redox states triggered by an electrical signal. To realize such applications, electrical switchable characteristics focusing on complexes **4** and **5** are in progress.

Supplementary Materials: The following are available online at http://www.mdpi.com/2312-7481/5/2/30/s1, Table S1: X-ray crystallographic data for **1**–**5**, Figure S1: IR spectra of **1**–**5**, Figure S2: Frequency dependence of ac susceptibilities under variable dc fields for **1**–**5**, Figure S3: Argand plots under variable dc fields for **1**–**5**, Figure S4: τ versus $1/T$ plots with fits using Equation (2) for **4** and **5**, Figure S5: τ versus $1/T$ plots with fits using Equation (3) for **4** and **5**, Table S2: Summary of dc magnetic fields dependent relaxation times and α values for **4**, Table S3: Summary of dc magnetic fields dependent relaxation times and α values for **5**, Table S4: Summary of temperature dependent relaxation times and α values for **4**, Table S5: Summary of temperature dependent relaxation times and α values for **5**, Figure S6: Cyclic voltammograms of **4** and **5**.

Author Contributions: R.I. conceived and designed the experiment. R.I. wrote the manuscript in consultation with co-authors; R.I., T.N., S.M., and S.K. executed syntheses and their characterization, and single-crystal X-ray diffraction measurements and their structure refinement; R.I., K.K., and M.Y. executed magnetic measurements. Ryuta Ishikawa analyzed all magnetic data.

Funding: This work was supported financially by the Ministry of Education, Culture, Sports, Science and Technology (MEXT) KAKENHI (Grant-in-Aid for Scientific Research on Innovative Areas), Grant Number 18H04529 "Soft Crystals" (Ryuta Ishikawa) and 17H05390 "Coordination Asymmetry" (Satoshi Kawata), as well as by the Japan Society for the Promotion of Science (JSPS) KAKENHI, Grant Number (Grant-in-Aid for Scientific Research (C)) 16K05735 (Satoshi Kawata). This work was also supported financially by the Central Research Institute of Fukuoka University, Grant Number 171041 (Ryuta Ishikawa) and 171011 (Satoshi Kawata).

Acknowledgments: Masahiro Yamashita thanks the support by the 111 project (B18030) from China. We would like to thank Editage (www.editage.jp) for English language editing.

Conflicts of Interest: The authors declare no conflict of interest.

References

1. Mannini, M.; Pineider, F.; Sainctavit, P.; Danieli, C.; Otero, E.; Sciancalepore, C.; Talarico, A.M.; Arrio, M.-A.; Cornia, A.; Gatteschi, D.; et al. Magnetic memory of a single-molecule quantum magnet wired to a gold surface. *Nat. Mater.* **2009**, *8*, 194–197. [CrossRef]
2. Leuenberger, M.N.; Loss, D. Quantum computing in molecular magnets. *Nature* **2001**, *410*, 789–793. [CrossRef]

3. Meier, F.; Levy, J.; Loss, D. Quantum computing with spin cluster qubits. *Phys. Rev. Lett.* **2003**, *90*, 47901–47904. [CrossRef] [PubMed]
4. Winpenny, R.E.P. Quantum information processing using molecular nanomagnets as qubits. *Angew. Chem. Int. Ed.* **2008**, *47*, 7992–7994. [CrossRef]
5. Chiesa, A.; Whitehead, G.F.S.; Carretta, S.; Carthy, L.; Timco, G.A.; Teat, S.J.; Amoretti, G.; Pavarini, E.; Winpenny, R.E.P.; Santini, P. Molecular nanomagnets with switchable coupling for quantum simulation. *Sci. Rep.* **2014**, *4*, 7423. [CrossRef] [PubMed]
6. Bogani, L.; Wernsdorfer, W. Molecular spintronics using single-molecule magnets. *Nat. Mater.* **2008**, *7*, 179–186. [CrossRef]
7. Camarero, J.; Coronado, E. Molecular vs. inorganic spintronics: The role of molecular materials and single molecules. *J. Mater. Chem.* **2009**, *19*, 1678–1684. [CrossRef]
8. Sanvito, S. Molecular spintronics. *Chem. Soc. Rev.* **2011**, *40*, 3336–3355. [CrossRef]
9. Clemente-Juan, J.M.; Coronado, E.; Gaita-Ariño, A. Magnetic polyoxometalates: From molecular magnetism to molecular spintronics and quantum computing. *Chem. Soc. Rev.* **2012**, *41*, 7464–7478. [CrossRef]
10. Rinehart, J.D.; Long, J.R. Exploiting single-ion anisotropy in the design of f-element single-molecule magnets. *Chem. Sci.* **2011**, *2*, 2078–2085. [CrossRef]
11. Sorace, L.; Benelli, C.; Gatteschi, D. Lanthanides in molecular magnetism: Old tools in a new field. *Chem. Soc. Rev.* **2011**, *40*, 3092–3104. [CrossRef]
12. Woodruff, D.N.; Winpenny, R.E.P.; Layfield, R.A. Lanthanide single-molecule magnets. *Chem. Rev.* **2013**, *113*, 5110–5148. [CrossRef] [PubMed]
13. Habib, F.; Murugesu, M. Lessons learned from dinuclear lanthanide nano-magnets. *Chem. Soc. Rev.* **2013**, *42*, 3278–3288. [CrossRef]
14. Liddle, S.T.; Van Slageren, J. Improving f-element single molecule magnets. *Chem. Soc. Rev.* **2015**, *44*, 6655–6669. [CrossRef] [PubMed]
15. Pointillart, F.; Cador, O.; Le Guennic, B.; Ouahab, L. Uncommon lanthanide ions in purely 4f Single Molecule Magnets. *Coord. Chem. Rev.* **2017**, *346*, 150–175. [CrossRef]
16. McAdams, S.G.; Ariciu, A.-M.; Kostopoulos, A.K.; Walsh, J.P.S.; Tuna, F. Molecular single-ion magnets based on lanthanides and actinides: Design considerations and new advances in the context of quantum technologies. *Coord. Chem. Rev.* **2017**, *346*, 216–239. [CrossRef]
17. Dey, A.; Kalita, P.; Chandrasekhar, V. Lanthanide(III)-based single-ion magnets. *ACS Omega* **2018**, *3*, 9462–9475. [CrossRef]
18. Zhu, Z.; Guo, M.; Li, X.-L.; Tang, J. Molecular magnetism of lanthanide: Advances and perspectives. *Coord. Chem. Rev.* **2019**, *378*, 350–364. [CrossRef]
19. Sessoli, R.; Tsai, H.L.; Schake, A.R.; Wang, S.; Vincent, J.B.; Folting, K.; Gatteschi, D.; Christou, G.; Hendrickson, D.N. High-spin molecules: $[Mn_{12}O_{12}(O_2CR)_{16}(H_2O)_4]$. *J. Am. Chem. Soc.* **1993**, *115*, 1804–1816. [CrossRef]
20. Sessoli, R.; Gatteschi, D.; Caneschi, A.; Novak, M.A. Magnetic bistability in a metal-ion cluster. *Nature* **1993**, *365*, 141–143. [CrossRef]
21. Abdus Subhan, M.; Kawahata, R.; Nakata, H.; Fuyuhiro, A.; Tsukuda, T.; Kaizaki, S. Synthesis, structure and spectroscopic properties of chloranilate-bridged 4f-4f dinuclear complexes: A comparative study of the emission properties with Cr-Ln complexes. *Inorg. Chim. Acta* **2004**, *357*, 3139–3146. [CrossRef]
22. Dunstan, M.A.; Rousset, E.; Boulon, M.-E.; Gable, R.W.; Sorace, L.; Boskovic, C. Slow magnetisation relaxation in tetraoxolene-bridged rare earth complexes. *Dalton Trans* **2017**, *46*, 13756–13767. [CrossRef] [PubMed]
23. Ishikawa, R.; Michiwaki, S.; Noda, T.; Katoh, K.; Yamashita, M.; Matsubara, K.; Kawata, S. Field-induced slow magnetic relaxation of mono- and dinuclear dysprosium(III) complexes coordinated by a chloranilate with different resonance forms. *Inorganics* **2018**, *6*, 7. [CrossRef]
24. Zhang, P.; Perfetti, M.; Kern, M.; Hallmen, P.P.; Ungur, L.; Lenz, S.; Ringenberg, M.R.; Frey, W.; Stoll, H.; Rauhut, G.; et al. Exchange coupling and single molecule magnetism in redox-active tetraoxolene-bridged dilanthanide complexes. *Chem. Sci.* **2018**, *9*, 1221–1230. [CrossRef] [PubMed]
25. Flanagan, B.M.; Bernhardt, P.V.; Krausz, E.R.; Lüthi, S.R.; Riley, M.J. A ligand-field analysis of the trensal (H_3trensal = 2,2′,2″-Tris(salicylideneimino)triethylamine) ligand. An application of the angular overlap model to lanthanides. *Inorg. Chem.* **2002**, *41*, 5024–5033. [CrossRef]

26. Quadrelli, E.A. Lanthanide contraction over the 4f series follows a quadratic decay. *Inorg. Chem.* **2002**, *41*, 167–169. [CrossRef] [PubMed]
27. Seitz, M.; Oliver, A.G.; Raymond, K.N. The lanthanide contraction revisited. *J. Am. Chem. Soc.* **2007**, *129*, 11153–11160. [CrossRef]
28. D'Angelo, P.; Zitolo, A.; Migliorati, V.; Chillemi, G.; Duvail, M.; Vitorge, P.; Abadie, S.; Spezia, R. Revised ionic radii of lanthanoid(III) ions in aqueous solution. *Inorg. Chem.* **2011**, *50*, 4572–4579. [CrossRef] [PubMed]
29. Casanova, D.; Llunell, M.; Alemany, P.; Alvarez, S. The rich stereochemistry of eight-vertex polyhedra: A continuous shape measures study. *Chem. Eur. J.* **2005**, *11*, 1479–1494. [CrossRef] [PubMed]
30. Llunell, M.; Casanova, D.; Cirera, J.; Bofill, J.M.; Alemany, P.; Alvarez, S. *SHAPE*; Version 2.1; University of Barcelona: Barcelona, Spain, 2013.
31. Kitagawa, S.; Kawata, S. Coordination compounds of 1,4-dihydroxybenzoquinone and its homologues. Structures and properties. *Coord. Chem. Rev.* **2002**, *224*, 11–34. [CrossRef]
32. Apostolidis, C.; Rebizant, J.; Kanellakopulos, B.; von Ammon, R.; Dornberger, E.; Müller, J.; Powietzka, B.; Nuber, B. Homoscorpionates (hydridotris(1-pyrazolyl)borato complexes) of the trivalent 4f ions. The crystal and molecular structure of $[(HB(N_2C_3H_3)_3)_3Ln^{III}$, (Ln = Pr, Nd). *Polyhedron* **1997**, *16*, 1057–1068. [CrossRef]
33. Sears, V.F. Neutron scattering lengths and cross sections. *Neutron News* **1992**, *3*, 26–37. [CrossRef]
34. Chen, Y.-C.; Liu, J.-L.; Wernsdorfer, W.; Liu, D.; Chibotaru, L.F.; Chen, X.-M.; Tong, M.-L. Hyperfine-interaction-driven suppression of quantum tunneling at zero field in a holmium(III) single-ion magnet. *Angew. Chem. Int. Ed.* **2017**, *56*, 4996–5000. [CrossRef]
35. Moreno-Pineda, E.; Damjanović, M.; Fuhr, O.; Wernsdorfer, W.; Ruben, M. Nuclear spin isomers: Engineering a $Et_4N[DyPc_2]$ spin qudit. *Angew. Chem. Int. Ed.* **2017**, *56*, 9915–9919. [CrossRef]
36. Kishi, Y.; Pointillart, F.; Lefeuvre, B.; Riobé, F.; Le Guennic, B.; Golhen, S.; Cador, O.; Maury, O.; Fujiwara, H.; Ouahab, L. Isotopically enriched polymorphs of dysprosium single molecule magnets. *Chem. Commun.* **2017**, *53*, 3575–3578. [CrossRef]
37. Flores Gonzalez, J.; Pointillart, F.; Cador, O. Hyperfine coupling and slow magnetic relaxation in isotopically enriched Dy^{III} mononuclear single-molecule magnets. *Inorg. Chem. Front.* **2019**. [CrossRef]
38. Cole, K.S.; Cole, R.H. Dispersion and absorption in dielectrics, I. alternating current characteristics. *J. Chem. Phys.* **1941**, *9*, 341–351. [CrossRef]
39. Guo, Y.-N.; Xu, G.-F.; Guo, Y.; Tang, J. Relaxation dynamics of dysprosium(iii) single molecule magnets. *Dalton Trans.* **2011**, *40*, 9953–9963. [CrossRef] [PubMed]
40. Gatteschi, D.; Sessoli, R.; Villain, J. *Molecular Nanomagnets*; Oxford University Press: Oxford, UK, 2006. [CrossRef]
41. *CrystalClear-SM*; Version 1.4.0 SP1; Rigaku and Rigaku/MSC: The Woodlands, TX, USA, 2008.
42. *CrystalStructure*; Version 4.2.2; Rigaku and Rigaku/MSC: The Woodlands, TX, USA, 2017.
43. Burla, M.C.; Caliandro, R.; Camalli, M.; Carrozzini, B.; Cascarano, G.L.; Giacovazzo, C.; Mallamo, M.; Mazzone, A.; Polidori, G.; Spagna, R. SIR2011: A new package for crystal structure determination and refinement. *J. Appl. Crystallogr.* **2012**, *45*, 357–361. [CrossRef]
44. Sheldrick, G.M. Crystal structure refinement with SHELXL. *Acta Crystallogr. Sect. C* **2015**, *71*, 3–8. [CrossRef]
45. Bain, G.A.; Berry, J.F. Diamagnetic corrections and Pascal's constants. *J. Chem. Educ.* **2008**, *85*, 532–536. [CrossRef]